Chiral Effects on Supraparticles for Controllable Nanomedicine

Jihyeon Yeom[1], **Pedro P. G. Guimaraes**[1,2], **Hyo Min Ahn**[3], **BoKyeong Jung**[3], **Quanyin Hu**[1], **Kevin McHugh**[1], **Michael J. Mitchell**[1,4], **Chae-Ok Yun**[3], **Robert Langer**[1,*], **Ana Jaklenec**[1,*]

[1]David H. Koch Institute for Integrative Cancer Research, Massachusetts Institute of Technology, Cambridge, MA 02139

[2]Department of Physiology and Biophysics, Institute of Biological Sciences, Universidade Federal de Minas Gerais, Belo Horizonte, MG, Brazil

[3]Department of Bioengineering, Hanyang University, Seoul, Republic of Korea

[4]Department of Bioengineering, University of Pennsylvania, Philadelphia, PA, United States

Abstract

Chirality is ubiquitous in nature and hard-wired into every biological system. Despite the prevalence of chirality in biological systems, controlling biomaterial chirality to influence interactions with cells has only recently been explored. Here, we present chiral-engineered supraparticles (SPs) that interact differentially with cells and proteins depending on their handedness. SPs coordinated with *D*- chirality demonstrated greater than three-fold enhanced cell membrane penetration in breast, cervical, and multiple myeloma cancer cells. We carried out quartz crystal microbalance with dissipation and isothermal titration calorimetry measurements to understand the mechanism of these chiral-specific interactions. Thermodynamically, *D*-SPs showed more stable adhesion to lipid layers composed of phospholipids and cholesterol compared to *L*-SPs. *In vivo*, *D*-SPs exhibited superior stability and longer biological half-lives likely due to opposite chirality and thus protection from endogenous proteins including proteases. This work showed that incorporating *D*-chirality into nanosystems enhanced uptake by cancer cells and prolonged *in vivo* stability in circulation, providing support for the importance of chirality in biomaterials. Thus, chiral nanosystems may have the potential to provide a new level of control for drug delivery systems, tumor detection markers, biosensors, and other biomaterial based devices.

Keywords

chirality; supraparticles; self-assembly; drug delivery system; nanomedicine

Introduction

Chirality is widely prevalent in nature, imparting uniqueness and specificity to the biological, chemical, mechanical, and optical properties of materials that have identical elemental compositions but are non-superimposable. Depending on the application, nature has selected one of two enantiomeric forms.[1–3] For example, evolution resulted in *L*- form amino acids and *D*- form sugars, RNA, and DNA as the main components of biological systems.[4,5] Due to chiral-specific interactions in biological systems, one enantiomer can serve an important biological function while the other enantiomer is inactive or even toxic [6,7]. Thus, molecular chirality has long been considered an important factor in the design of drugs, pharmacology, toxicology, pharmacokinetics, and metabolism,[8,9] with most drugs being manufactured in an enantiomerically pure form that is biologically active and safe. [10,11]

In contrast to molecular chirality, supramolecular chirality and its potential role in biology has yet to be fully explored and remains poorly understood.[12,13] Since the functionality of biological systems is often closely related to their physical structure, chirality is likely to be important in nanomedicine and therefore merits consideration when designing new biomaterials.[14–16] Most supramolecular biomolecules, such as lipids, and glycans, can change their properties depending on their chirality.[17–19] In human sensory processing, molecules that are consumed or reach the olfactory receptors can taste sweet or bitter and smell differently depending on their chirality.[20,21] These chiral-sensitive receptors are not limited to just the tongue and nose, but rather are present in the stomach, intestine, and pancreas as well, which can significantly affect metabolism.[22] Likewise, chiral supramolecules are critically involved in many physiological changes in the body and their dysfunction may contribute to diseases such as cancer, diabetes and obesity.[23,24] The geometric isomerism also governs physiological and physical properties of fatty acids that significantly affect signaling responses, aging, and health impairments. [25]

Based on these examples, chiral nanotechnology can be strategically implemented in developing new biomaterials. For example, site-specific interactions between DNA and chiral quantum dots demonstrated photo-induced cleavage of DNA strains, which suggests that chiral nanostructures may be useful as a gene editing tools.[26] Some drug delivery systems (DDS) also fall into a size range similar to naturally occurring chiral supra-biomolecules.[27] There are several requirements that new materials should satisfy in order to be efficient nano-DDS. They need to (1) have efficient adhesion to biological surfaces such as cellular membranes, (2) resist enzymatic digestion to ensure efficient blood circulation, (3) degrade into components less than 4 nm in size to enable renal clearance, (4) possess a reasonably high drug carrying capacity via porosity or a high surface area-to-volume ratio.

In order to address the first requirement, we chose to create right-handed DDS with the hypothesis that this chirality would match the handedness of phospholipids in the cell membrane and therefore lead to higher cell membrane binding affinity.[28] To prevent enzymatic clearance and increase circulation time (requirement 2), we developed DDS with *D*-amino acids on their surface to minimize interaction with enzymes, which are composed

of *L*- amino acids, since previous research has shown that stuctures with this alternative chirality demonstrate superior resistance to enzymatic digestion.[16,29] Providing *D*- chirality on NPs also brings higher tumor eradication efficiency.[30] The need for appropriate clearance from the body (requirement 3) and high drug loading (requirement 4) are typically opposing design elements, as small particle sizes are excreted by the kidney, but are also correlated with poor drug loading and retention. To create a DDS with both favorable properties, we assembled supra-nanostructures from small chiral nanoparticles (NPs) that can disassemble and be cleared from circulation while increasing drug loading and retention. Self-assembly of NPs is a powerful tool that enables the formation of complex suprastructures with fine control over size, structure, and function.[31] Supraparticles (SPs) formed with nanometer size inorganic NPs stabilized by amino acids have advantages compared to solid NPs of the same size, due to the high surface area and porosity enabling efficient multi-functionality and drug loading. Efforts to develop highly organized SPs through self-assembly of NPs for various applications have shown that repulsive interactions and attractive forces mediate the self-assembly process.[32–34]

In particular, there have been several groups studying chiral gold NPs for biochemical applications.[35] Using the strong binding affinity between gold and thiol, thiol-containing molecules such as glutathione have been actively used as the chirality providing ligands on these NPs.[1,36] The resulting NPs exhibited optical activity not only in the UV region, where it is absorbed by the organic molecules, but also in the visible range where the surface plasmonic resonance absorbance occurs, imparting chirality from the ligands to the core. However, due to the flexibility of the gold-sulfur interface, it has been reported that chiral gold NPs undergo racemization at modest temperatures (40–80 °C)[37] and even inversion of chirality with the exposure to the opposite enantiomer[38]. In order to fully examine chirality effects of nanostructures in the biological environment, a reliable system that maintains its chirality is desired. Thus, using cobalt oxide based NPs is preferred since they are known to conserve their chirality even when the ligands on the surface are exchanged to different molecules. For example, it has been demonstrated that cobalt oxide NPs synthesized using *L*-cysteine showed little change on CD spectra even after the *L*-cysteine on the surface was exchanged to *D*-penicillamine [2].

Here we report the synthesis of chiral SPs by assembling 2–3 nm cobalt oxide NPs capped with *L*-, *D*-, or *DL*- cysteine via a modified method[2] (Figure 1A and S1–3). In addition to the reported synthesis method,[2] we added dithiol poly(ethylene glycol) (PEG) and PEG methyl ether to drive attractive and repulsive competing interactions between NPs that can lead to both self-assembly and self-terminating SPs. Owing to the strong binding between cobalt and the thiol functional groups at both ends of PEG, dithiol PEG works as a cross-linker contributing to SP growth. PEG methyl ether that possesses methyl and hydroxyl groups at each end of PEG polymer provides slightly repulsive interactions between building block NPs. Hydroxyl groups also have an affinity for cobalt that leads to methyl group exposure on the surface. The slight hydrophobicity of the methyl groups[39,40] competes with the attractive dithiol PEG. The significant contribution of PEG end-group hydrophobicity on molecular interactions in aqueous solution has been also demonstrated elsewhere. [41] Due to the end-group effect, the SP growth then terminates when the system reaches a thermodynamic equilibrium. In our system, growth and self-assembly occurred

spontaneously in the aqueous phase at room temperature for two hours, at which time SPs achieved a size of approximately 60 nm when equimolar amounts of dithiol PEG and PEG methyl ether were used (Figure 1B). Elemental composition analysis performed using energy dispersive spectroscopy (EDAX) showed that SPs were composed of 21 % Co, 32 % O, and 47 % S atoms (Table S1). The detected sulfur was from thiols in cysteine. When synthesis was performed with dithiol PEG in 3-fold molar excess compared to PEG methyl ether, the resulting product was an inter-connected chain structure rather than discrete SPs (Figure 1C left). When the opposite ratio of 1 to 3 dithiol PEG to PEG methyl ether was used, smaller and irregular shaped SPs were obtained (Figure 1C right). These results indicate that SP size can be controlled by the ratio of the two attractive and repulsive competing polymers, in this case, dithiol PEG and PEG methyl ether (Figure S3).

Importantly, this self-assembling, self-terminating process did not affect the chirality of the nanostructures as confirmed by identical circular dichroism (CD) signals from small NPs and assembled SPs (Figure 1D). We obtained strong optical activity throughout the UV and visible regions of the CD spectra. The average size and concentration were measured by nano-flow cytometry (Figure 1E). Since lipids are the main component of the cellular membrane and known to be chiral, we also evaluated the optical activity of lipids extracted from human bone marrow endothelial cells (HBMEC) and breast cancer cells (MBA-MB-231). Lipids from both cell lines showed a positive CD signal at around 270 nm (Figure 1F) where *D*-cysteine-capped SPs (*D*-SPs) showed a strong positive peak whereas *L*-cysteine-capped SPs (*L*-SPs) showed a strong negative signal (Figure 1D). Since the attractive interaction between the structures that possess the same optical activity is stronger than that between opposite optical isomeric structures,[28] we hypothesized that *D*-SPs will interact with cellular membrane more effectively than *L*-SPs. In this study, the role of the building block NPs was important as a platform tethering cysteines on a surface that tightly compacts the chiral molecules in a confined space. When *L*-, *D*-, and *DL*-cysteine were dispersed in the media without NPs, the molecules did not show dramatic differences in cell viability depending on their chirality regardless of the concentration (Figure S4). Additionally, the relatively larger SPs that are about 60 nm were used to examine the selective chiral effects by preventing cytotoxicity from the very small NP (2–3nm) building blocks. It has been reported that the size of NPs greatly affects their cytotoxicity. For example, silver NPs with 4.7 nm size showed dramatically higher cytotoxicity than 42 nm NPs[42], and silica NPs with 20 nm size showed much higher toxicity than 60 nm NPs[43]. Indeed, the small NP building blocks, 2–3 nm, showed much higher toxicity; thus their chiral selective interactions were not distinguishable (Figure S5). This size effect was also confirmed by QCM-D measurement. Both *L*- and *D*-NPs showed absorption on the lipid bilayer without chiral specificity (Figure S7). Thus, in order to evaluate the chiral effect without the interference of the size effect, the assembly into SPs was necessary.

To understand chiral-specific interactions between SPs and cells, we evaluated SP internalization quantitatively and qualitatively using flow cytometry and confocal microscopy. We exposed cells to fluorescently labeled SPs for 24 hours, performed a series of rinses to remove unbound SPs and then quantified the cellular uptake of SPs via confocal microscopy. Interestingly, the fluorescence from internalized *D*-SPs was 3- to 4-fold stronger than that from internalized *L*-SPs cells (Figure 2 A and B). Since it is not readily

possible to distinguish between internalization and cell surface association using flow cytometry alone, we also carried out confocal imaging. From these images, we found that a noticeably higher number of *D*-SPs were internalized compared to *L*- and *DL*-SPs (Figure 2 C–F). To quantitatively compare the amount of chiral SPs internalized in cells, we calculated the averaged integrated two dimensional pixel numbers per area of the red channel using ImageJ software. About 3-fold more *D*-SPs were internalized to the cells than *L*-SPs. This trend is well correlated with the flow cytometry results (Figure 2B).

To determine the toxicity of SPs after the internalization, we carried out cell viability experiments using cervical cancer cells (HeLa), breast cancer cells (MBA-MD-231), multiple myeloma cells (MM. 1S), and breast cancer cells (SKBR3) after exposure to chiral SPs for 24 hours (Figure 3A and S8). As expected, *D*-SPs included greater levels of cytotoxicity than *L*- and *DL*-SPs, which we hypothesize is due to the 3-fold increase in the internalization of *D*-SPs. To determine whether the decrease in viability was through an apoptotic pathway, fluorescence-activated cell sorter (FACS) analysis was performed on annexin-FITC and propidium iodide (PI) double-stained cells. Intact cells (annexin-/PI-) can be discriminated from apoptotic cells (annexin+/PI-), and necrotic cells (annexin+/PI+) as seen in Figure 4A–C. While greater than 90 % of cells were alive after exposure to *L*- and *DL*- SPs, only 24.5 % of cells were shown to be alive with *D*-SPs. Cell death resulting from *D*-SPs was mainly via apoptosis, as indicated by high annexin+/ PI- signals (Figure 3C). To further support that chiral SPs induced apoptosis, we treated cells with caspase inhibitors prior to SP exposure. Since caspase is a key enzyme involved in apoptosis, inhibiting caspase activity prevents apoptotic cell death. After treatment with the caspase inhibitor, Z-VAD, cell viability did not decrease with SPs incubation suggesting that apoptosis was the dominant mechanism of SP-induced cell death (Figure 3B). Although many sources of cellular damage can trigger caspase activation, the disruption of the mitochondrial membrane is one of the most common triggers of apoptosis via cytochrome C activation of caspase. After staining cells with Mitotracker dye staining, approximately 26% of cells exposed to *D*-SPs exhibited green fluorescence consistent with apoptosis, whereas only 5.9% and 12.6 % of cells displayed this apoptosis marker when treated with *L*- and *DL*-SPs, respectively (Figure 3D). Taken together, these results suggest that *D*-SP-induced cell death is predominantly triggered by apoptosis through mitochondrial membrane damage.

To understand the interactions between chiral SPs and cell membranes in real time, we performed a quartz crystal microbalance with dissipation (QCM-D) measurements. We hypothesized that stronger adhesion of *D*-SPs to cellular membrane components would lead to greater cell internalization. We first formed supported lipid bilayers (SLBs) to mimic cell membrane structure through a liposome fusion method on the SiO$_2$-coated quartz crystal surface and then monitored SPs absorption on SLBs. Liposomes for SLB formation were prepared in advance using phosphatidylcholine and cholesterol with the weight ratio of 3:1 by the extrusion method. The final size of the liposomes was 70 nm.

The prepared liposomes in buffer (150 mM NaCl, 10 mM HEPES, and 1 mM MgCl$_2$) were slowly injected into the quartz crystal in the QCM-D system. As soon as the liposomes absorbed on the crystal, the frequency decreased, reflecting an increase in mass, and the dissipation increased, reflecting an increase in viscosity, denoting a soft film formation

(Figure 4 A and B). The frequency then sharply increased due to the loss of unbound lipid molecules and solvent trapped inside liposomes. The replacement of liquids inside and in-between liposomes with more rigid lipid molecules led to a significant decrease in dissipation, indicating that the liposomes spontaneously fused and formed the planar supported bilayer. After flowing buffer to remove loosely bound lipid molecules on the crystal, we replaced the running solvent with a solution containing N-2-hydroxyethylpiperazine-N′–2-ethanesulphonic acid (HEPES) in order to prepare for SP administration. Chiral *D*- or *L*-SPs in HEPES were injected to the system with a flow rate of 150 μL/min. The number of NPs added was held constant for both *D*- and *L*-SPs. The changes in frequency and dissipation shifts observed reflect the interactions between SPs and the lipid bilayer. With *L*-SPs administration, the changes in both mass and viscosity (Figure 4B and 4D) were insignificant as the frequency varied by only 0.2 Hz and no detectable differences were observed with dissipation suggesting only very weak interactions between *L*-SPs and the SLBs. In the case of *D*-SPs, the frequency decreased noticeably with the degree of 2 Hz indicating that the mass on the crystal increased (Figure 4A and 4C). The dissipation also slightly decreased, revealing an increased rigidity of the layer due to the replacement of soft lipid molecules to rigid inorganic SPs of the film. The results from the QCM-D study indicated that *D*-SPs have about 10 times stronger affinity and more efficient absorption to SLBs than *L*-SPs (Figure 4A–D).

To confirm the chirality-specific interactions in a thermodynamic manner, we carried out isothermal titration calorimetry (ITC) measurements while adding *L*- or *D*-SPs into a liposome dispersion (Figure 4C–F). Liposomes were prepared through the same extrusion method, but the final size was around 800 nm. Although the three types SPs showed an overall favorable enthalpy change with negative free energy, the affinity between liposomes and *D*-SPs was two-fold more energetically favorable than with *L*- or *DL*-SPs in terms of Gibbs free energy. The association constant K value for *D*-SPs was about 40 M^{-1} which is 56-fold higher than that from *L*-SPs (~ 0.72 M^{-1}), thus confirming the significantly stronger affinity of *D*-SPs to liposomes than that of *L*-SPs.

Control over DDS degradation is important for efficient drug delivery and renal clearance. Using a near Infra-Red fluorescent dye covalently bound to SPs, we evaluated SPs clearance from the body over time to understand chiral-specific biological interactions *in vivo*. Chiral SPs were administered intravenously in mice with a dose of 5 mg/kg. 30 min, 2 hours and 24 hours after injection, we measured SP fluorescence using a non-invasive imaging system. At 30 min, the fluorescence intensity from *L*-, *D*-, and *DL*- SPs were not statistically different (Figure 5A and 5B). From the images obtained 2 hours after injection, *D*-SPs clearly showed prolonged retention in the body, which also resulted in broader distribution in the body. After 24 hours, most *L*-SPs were excreted while a significant amount of *D*-SPs still remained. It has been shown that the major excretion routes of NPs from the body are through renal (kidney) or hepatic (liver) excretion into urine and feces [44,45] Since these pathways rely on glomerular filtration in the kidney and liver, these processes are mainly affected by the size of NPs. When the hydrodynamic diameter is less than ~ 5 nm, the NPs show rapid and efficient excretion from the body. [44,45] To check the size-dependent clearance of nanostructures, we studied the SPs distribution in organs in mice. The results

indicate that most of the remaining SPs were trapped in liver and kidney (Figure 5C and 5D).

Importantly, because *DL*-SPs with an equal proportion of *D*- and *L*-SPs demonstrated behavior that was between that of pure *L*- and *D*-SPs. The ability of chirality to affect blood plasma half-life was also examined by measuring fluorescent signals from SPs in blood plasma sampled from each mice at various time points post injection (Figure 5E). We calculated the concentrations of SPs remained in blood based on the fluorescence intensities and particle numbers measured by nano-flow cytometry. As we expected, *L*-SPs showed the fastest decrement when *D*-SPs showed the slowest clearance rate.

To understand the chirality-dependent body clearance rates, we loaded a model drug molecule, a fluorescent dye conjugated dextran (dextran-FITC, 70 kDa) during the SPs self-assembly. The molecule was loaded by topological entanglement within the network not through covalent bonds so that when the network is degraded, the molecule can be released (Scheme S1). By measuring the fluorescent intensities of escaped molecules, we could track the degradation of the SPs that lead to drug molecule release. After removing non-captured dextran-FITC molecules using 100 kDa membrane, we incubated the SPs in human plasma that contains protease at 37°C and then used a 100 kDa filter to separate released dextran-FITC from SPs at various incubation time points, and then measured the fluorescent signal. As expected, SPs with *D*- handedness showed stronger stability in human plasma (Figure 5F). The disassembly ratio between *L*- and *D*- SPs became obvious that *L*-SPs released about 10 % more amount of dex-FITC after 12 hours of incubation, and it further increased to over 40 % after 24 hours of incubation. These results reveal that the slower removal of *D*-SPs from the body was due to the higher stability against enzymatic digestions. In contrast to SPs, the dispersed NP building blocks without the covalent linker could not load any dex-FITC. We can infer that the biological half-life of these nanosystems can in part be modulated by their chirality.

In conclusion, we explored the chirality effects of nanostructures to control interactions with biological systems. We synthesized chiral SPs through self-limiting assembly by manipulating the attractive and repulsive interactions between NP building blocks. During the synthesis, *L*- and *D*- cysteine were used as chirality providing agents. Due to the stronger affinity between the same optical isomeric systems, SPs capped by *D*-cysteine showed a higher attractive and adhesive interaction with cellular membranes that are composed mainly with lipid molecules, leading to a 3 to 4-fold increase in cell internalization. When it comes to blood that contains a large, heterogeneous population of proteins, SPs capped by *D*-cysteine showed superior stability and longer biological half-lives due to the incompatible chirality with endogenous proteins including proteases. This study shows that incorporating *D*-chirality into nanosystems enhances cellular uptake and *in vivo* stability in blood providing support for the importance of chirality in bioengineering new materials. As a result, chiral nanosystems may have the potential to provide a new level of control for DDS, tumor detection markers, biosensors, and potentially other biomaterial devices.

Materials and methods

Chiral SP synthesis and characterization

SPs were synthesized following the slightly modified reported method [2] using cobalt (II) chloride and *L*-, *D*- or *DL*- cysteine as chiral and achiral agents. In 47.3 mL of E-pure water, we added 2 mL of 100 mM *L*-, *D*- or *DL*- cysteine, 100 mg PEG methyl ether (Mw 2000), 75 mg of dithiol PEG (Mw 1500), 200 μL of 500 mM $NaBH_4$, and 500 μL of 400 mM $CoCl_2$. All chemicals were purchased from Sigma-Aldrich. After two hours of magnetic stirring at room temperature, dark brownish transparent dispersions were obtained. The synthesized SPs were analyzed after sufficient purifications by dialysis using a 12–14 kDa MWCO membrane against E-pure water. TEM analysis was performed with JEOL 2010f using copper coated carbon TEM grids. UV-vis absorption and CD spectra measurements were done using JASCO 1700. SPs concentration was measured using nano-flow cytometry (nCS1, Spectradyne LLC).

Cell lines and cell culture

RMPI 1640 and Dulbecco's modified Eagle's medium (Gibco, Grand Island, NY) supplemented with 10% fetal bovine serum (FBS; Gibco), *L*-glutamine (2 mmol/L), penicillin (100 IU/mL), streptomycin (50 mg/mL), and 10 mM HEPES (4-(2-hydroxyethyl)-1-piperazineethanesulfonic acid) buffer was used as the culture medium. HeLa (human cervical carcinoma cell line HBMEC (human bone marrow endothelial cells), MM. 1S (human multiple myeloma cells), SKBR3 (human breast cancer cells) and MDA-MB-231 (human breast cancer cell line) were obtained from the American Type Culture Collection (ATCC; Manassas, VA). The cells were incubated at 37°C in a 5% CO_2 atmosphere. All cell lines tested negative for *Mycoplasma* when tested by Hoeschst dye (MP Biomedicals, Irvine, CA) staining, cell culture, and polymerase chain reaction.

Cell viability Assay

Cell viability experiments were carried out in a 96-well format with 4 replicates. Cells were plated at a density of 5×10^4 cells per well. At 24 h following cell seeding, cells were treated with *L*-, *D*-, or *DL*-SPs (4.3×10^8 particles/mL) for 48 hr at 37°C in a 5% CO_2 atmosphere and then assayed by using the ATP CellTiter-Glo® luminescent cell viability assay (Promega, Madison, WI) according to the manufacturer's protocol. Luminescence intensity was measured using a microplate reader (Infinite M200, Tecan, Austria).

For assays investigating apoptosis inhibition, cells were incubated with 20 μM Z-VAD-fmk for 4 hr prior to the addition of SPs. After being treated with *L*-, *D*-, and *DL*-SPs (1.7×10^8 particles/mL) for 48 hr, cell viability assay was measured using the ATP CellTiter-Glo® luminescent cell viability assay.

Apoptosis rate assays

Apoptotic cell death was determined using a dead cell apoptosis kit (Invitrogen, Carlsbad, CA) with fluorescein isothiocyanate (FITC) Annexin V and propidium iodide (PI) for flow cytometry according to the manufacturer's instructions. Cells were harvested after being treated with *L*-, *D*-, and *DL*-SPs (1.7×10^8 particles/mL) for 48 hr and washed with cold

PBS twice. After washing, cells were resuspended in 1× Annexin V binding buffer. Then, 5 μL of FITC Annexin V and 1 μL of 100 μg/mL PI working solution were added to each 100 μL of cell suspension and incubated at room temperature for 15 min. After the incubation period, an additional 500 μL of 1× Annexin binding buffer was added. Samples were then kept on ice until flow cytometry analysis.

QCM-D measurement

For QCM-D (Q-sense E4, Sweden) measurement, silicon dioxide coated crystals (QSX 303) were used. Lipid-bi-layers was formed on the crystal through adsorption and rupture of liposomes. Liposomes were prepared by the well-known extrusion method. [46] Briefly, cholesterol 5 mg and phosphatidylcholine (Avanti Polar Lipids, INC) 15 mg was dissolved in 600 uL chloroform in a glass tube and gently dried under nitrogen. To ensure complete removal of chloroform, the lipids were left under vacuum for an additional 12 h. The lipid film was hydrated with a liposome buffer composed of 150 mM NaCl, 10 mM HEPES, and 1 mM $MgCl_2$ dissolved in nuclease-free water. The resulting multilamellar liposomes were sized by repeated thawing and freezing, and then subjected to 15 extrusion cycles (Mini-Extruder, Avanti Polar Lipids Inc., USA) at 60 °C through different pore size polycarbonate membranes to produce unilamellar liposomes. The pore size of the filter used for the last extrusion was 50 nm. The liposome solution (0.1 mg/mL), buffers and SPs solutions were injected into the QCM-D system at a flow rate of 150 uL/min. The concentration of injected SPs was 1×10^7 particles/ mL.

The quartz crystal placed between two gold electrodes oscillates at its fundamental resonant frequency when a radio frequency voltage is applied. The resonant frequency of the crystal can be calculated by solving the wave equation which mostly decided by the dimensions. When we assume the quartz crystal as a cylinder whose radius is significantly greater than the thickness, $r_q \gg h_q$, the shear frequency f_n can be described as

$$f_n \approx \frac{v}{2\pi}\sqrt{\frac{n^2\pi^2}{h_q^2}} = \frac{nv}{2h_q} = nf_0 \qquad \text{(Eq. 1)}$$

where $n = 1,3,5,\cdots$, $v = \sqrt{\mu_q/\rho_q}$, μ_q and ρ_q are the shear modulus and the density of the crystal, and f_0 is the fundamental resonant frequency.[47,48] If a thin layer absorbed on the crystal, the thickness changes from h_q to h'_q, then the frequency also changes from f_n to f'_n. When $\Delta h_q = h_q - h'_q \ll h_q$, the negative proportional relationship between frequency shift and mass change $\left(\Delta M_q\right)$ can be described as following.[49,50]

$$\frac{\Delta f}{f_n} \approx \frac{\Delta h_q}{h_q} = -\frac{\Delta h_q \rho_q A_q}{h_q \rho_q A_q} = -\frac{\Delta M_q}{h_q \rho_q A_q} \qquad \text{(Eq. 2)}$$

The dissipation is related to the viscoelasticity of the film since it can be described with the loss and storage modulus as $D = G''/(2\pi G')$. [48]

Isothermal titration calorimetry measurement

Calorimetric titrations were carried out using a MicroCal PEAQ-ITC Isothermal Titration Calorimetry (ITC) Microcalorimeter (Malvern Panalytical, Malvern, UK) at 25°C. Each titration experiment consisted of 19 successive injections of D-, L- or DL-SPs (3.4×10^7 particles/mL) in buffer solution (pH 7.2) into the reaction cell charged with 400 μL of liposomes (2 mM) in the same buffer solution, with time intervals of 360s. The first injection (1.0 μL) was discarded to eliminate diffusion effects of material from the syringe to the reaction cell. Subsequent injections were used at a constant volume of 2.0 μL of liposomes. The time of injection was 2.0 s. The raw data was analyzed using the "one site model" set forth by Microcal Origin 7.0 for ITC.

Animal study-biodistribution

The biodistribution studies of SPs both *in vivo* and *ex vivo* were performed on female NOD/SCID (Charles River, Wilmington, MA) using an in-vivo imaging system (IVIS) (Perkin Elmer, Waltham, MA) Alexa 647 conjugated-SPs were injected intravenously (n = 5) at 5 mg/kg with PBS as a negative control (n = 3). Whole body and harvested tissues were imaged with IVIS. Fluorescent images were obtained from the anesthetized mice after 0.5 hr, 2 hr, and 24 hr using the IVIS imaging system (PerkinElmer, Hopkinton, MA). After 24 hr, mice were sacrificed and the organs were isolated (liver, heart, kidney, spleen, pancreas, lung, and, brain) and imaged.

SPs degradation in human plasma

During the SPs synthesis described above, we added 1 mg of dextran-FITC (70 kDa) to the reaction. After the complete synthesis following the aforementioned method, the product was sufficiently purified by dialysis against ultrapure water using 100 kDa membrane. Human plasma was purchased from Sigma-Aldrich. Using a 24 well plate, 3×10^6 SPs were added to 200 uL of human plasma solutions (n=5) in each well. The plate was placed in a cell culture incubator (37 °C) for 6, 12 and 24 hours. Before and after the incubation, we separated free dextran-FITC from SPs using centrifugal filters (100 kDa.) The FITC intensities of obtained supernatant were measured using a plate reader.

Supplementary Material

Refer to Web version on PubMed Central for supplementary material.

Acknowledgments

References

[1]. Lee H-E, Ahn H-Y, Mun J, Lee YY, Kim M, Cho NH, Chang K, Kim WS, Rho J, Nam KT, Nature 2018, 556, 360. [PubMed: 29670265]

[2]. Yeom J, Santos US, Chekini M, Cha M, De Moura AF, Kotov NA, Science 2018, 359, 309. [PubMed: 29348234]

[3]. Brandt JR, Salerno F, Fuchter MJ, Nat. Rev. Chem 2017, 1, 45.

[4]. Kumar A, Capua E, Kesharwani MK, Martin JML, Sitbon E, Waldeck DH, Naaman R, Proc. Natl. Acad. Sci 2017, 114, 2474. [PubMed: 28228525]

[5]. Nemati A, Shadpour S, Querciagrossa L, Li L, Mori T, Gao M, Zannoni C, Hegmann T, Nat. Commun 2018, 9, 3908. [PubMed: 30254259]

[6]. Hutt AJ, Tan SC, Drugs 1996, 52, 1.

[7]. Agranat I, Caner H, Caldwell J, Nat. Rev. Drug Discov 2002, 1, 753. [PubMed: 12360254]

[8]. Xue YP, Cao CH, Zheng YG, Chem. Soc. Rev 2018, 47, 1516. [PubMed: 29362736]

[9]. García-Guirado J, Svedendahl M, Puigdollers J, Quidant R, Nano Lett 2018, 18, 6279. [PubMed: 30216716]

[10]. Zhou Q, Yu LS, Zeng S, Drug Metab. Rev 2014, 46, 283. [PubMed: 24796860]

[11]. Nguyen LA, He H, Pham-Huy C, Int. J. Biomed. Sci 2006, 2, 85. [PubMed: 23674971]

[12]. Wang PP, Yu SJ, Govorov AO, Ouyang M, Nat. Commun 2017, 8, 1. [PubMed: 28232747]

[13]. Cecconello A, Besteiro LV, Govorov AO, Willner I, Nat. Rev. Mater 2017, 2, 17039.

[14]. Purcell-Milton F, McKenna R, Brennan LJ, Cullen CP, Guillemeney L, Tepliakov NV, Baimuratov AS, Rukhlenko ID, Perova TS, Duesberg GS, Baranov AV, Fedorov AV, Gun'Ko YK, ACS Nano 2018, 12, 954. [PubMed: 29338193]

[15]. Kong XT, Besteiro LV, Wang Z, Govorov AO, Adv. Mater 2018, 1801790.

[16]. Green DW, Lee J-M, Kim E-J, Lee D-J, Jung H-S, Adv. Mater. Interfaces 2016, 3, 1500411.

[17]. Dube DH, Bertozzi CR, Nat. Rev. Drug Discov 2005, 4, 477. [PubMed: 15931257]

[18]. Fuster MM, Esko JD, Nat. Rev. Cancer 2005, 5, 526. [PubMed: 16069816]

[19]. Gibaud T, Barry E, Zakhary MJ, Henglin M, Ward A, Yang Y, Berciu C, Oldenbourg R, Hagan MF, Nicastro D, Meyer RB, Dogic Z, Nature 2012, 481, 348. [PubMed: 22217941]

[20]. Temussi PA, Trends Biochem. Sci 2009, 34, 296. [PubMed: 19443222]

[21]. Gabriel AMS, Flavour 2015, 4, 1.

[22]. Trivedi BP, Nature 2012, 486, S7.

[23]. Beloribi-Djefaflia S, Vasseur S, Guillaumond F, Oncogenesis 2016, 5, e189.

[24]. Hilvo M, Denkert C, Lehtinen L, Müller B, Brockmöller S, Seppänen-Laakso T, Budczies J, Bucher E, Yetukuri L, Castillo S, Berg E, Nygren H, Sysi-Aho M, Griffin JL, Fiehn O, Loibl S, Richter-Ehrenstein C, Radke C, Hyötyläinen T, Kallioniemi O, Iljin K, Orešič M, Cancer Res 2011, 71, 3236. [PubMed: 21415164]

[25]. Chatgilialoglu C, Ferreri C, Melchiorre M, Sansone A, Torreggiani A, Chem. Rev 2014, 114, 255. [PubMed: 24050531]

[26]. Sun M, Xu L, Qu A, Zhao P, Hao T, Ma W, Hao C, Wen X, Colombari FM, de Moura AF, Kotov NA, Xu C, Kuang H, Nat. Chem 2018, 10, 821. [PubMed: 30030537]

[27]. Hao C, Xu L, Kuang H, Xu C, Adv. Mater 2019, 1802075.

[28]. Feng W, Kim JY, Wang X, Calcaterra HA, Qu Z, Meshi L, Kotov NA, Sci. Adv 2017, 3, 1.

[29]. Wade D, Boman A, Wåhlin B, Drain CM, Andreu D, Boman HG, Merrifield RB, Proc. Natl. Acad. Sci. U. S. A 1990, 87, 4761. [PubMed: 1693777]

[30]. Yuan L, Zhang F, Qi X, Yang Y, Yan C, Jiang J, Deng J, J. Nanobiotechnology 2018, 16, 55. [PubMed: 29996877]

[31]. Yeom J, Yeom B, Chan H, Smith KW, Dominguez-Medina S, Bahng JH, Zhao G, Chang WS, Chang SJ, Chuvilin A, Melnikau D, Rogach AL, Zhang P, Link S, Král P, Kotov NA, Nat. Mater 2015, 14, 66. [PubMed: 25401922]

[32]. Park J. Il, Nguyen TD, de Queirós Silveira G, Bahng JH, Srivastava S, Zhao G, Sun K, Zhang P, Glotzer SC, Kotov NA, Nat. Commun 2014, 5, 3593. [PubMed: 24845400]

[33]. Xia Y, Nguyen TD, Yang M, Lee B, Santos A, Podsiadlo P, Tang Z, Glotzer SC, Kotov NA, Nat. Nanotechnol 2011, 6, 580. [PubMed: 21857686]

[34]. Piccinini E, Pallarola D, Battaglini F, Azzaroni O, Mol. Syst. Des. Eng 2016, 1, 155.

[35]. Collins JT, Kuppe C, Hooper DC, Sibilia C, Centini M, Valev VK, Adv. Opt. Mater 2017, 5, 1700182.

[36]. Pigliacelli C, Sanjeeva KB, Nonappa A. Pizzi A. Gori, Bombelli FB, Metrangolo P, ACS Nano 2019, 13, 2158. [PubMed: 30649859]

[37]. Knoppe S, Dolamic I, Bürgi T, J. Am. Chem. Soc 2012, 134, 13114.

[38]. Gautier C, Bürgi T, J. Am. Chem. Soc 2008, 130, 7077. [PubMed: 18459786]

[39]. Koga Y, Westh P, Nishikawa K, Subramanian S, J. Phys. Chem. B 2011, 115, 2995. [PubMed: 21384939]

[40]. Vugmeyster L, Ostrovsky D, Ford JJ, Lipton AS, J. Am. Chem. Soc 2010, 132, 4038. [PubMed: 20201523]

[41]. Priya MH, Pratt LR, Paulaitis ME, Langmuir 2011, 27, 13713.

[42]. Avalos A, Haza AI, Mateo D, Morales P, J. Appl. Toxicol 2014, 34, 413. [PubMed: 24243578]

[43]. Kim I-Y, Joachim E, Choi H, Kim K, Nanomedicine Nanotechnology, Biol. Med 2015, 11, 1407.

[44]. Choi H. Soo, Liu W, Misra P, Tanaka E, Zimmer JP, Ipe B. Itty, Bawendi MG, Frangioni JV, Nat. Biotechnol 2007, 25, 1165. [PubMed: 17891134]

[45]. Yu M, Zheng J, ACS Nano 2015, 9, 6655. [PubMed: 26149184]

[46]. Bisso PW, Gaglione S, Guimarães PPG, Mitchell MJ, Langer R, ACS Biomater. Sci. Eng 2018, 4, 4255. [PubMed: 31497639]

[47]. Cho N-J, Frank CW, Kasemo B, Höök F, Nat. Protoc 2010, 5, 1096. [PubMed: 20539285]

[48]. Bailey CM, Kamaloo E, Waterman KL, Wang KF, Nagarajan R, Camesano TA, Biophys. Chem 2015, 203–204, 51.

[49]. Lu C, Czanderna AW, Applications of Piezoelectric Quartz Crystal Microbalances, Elsevier Science, 1984.

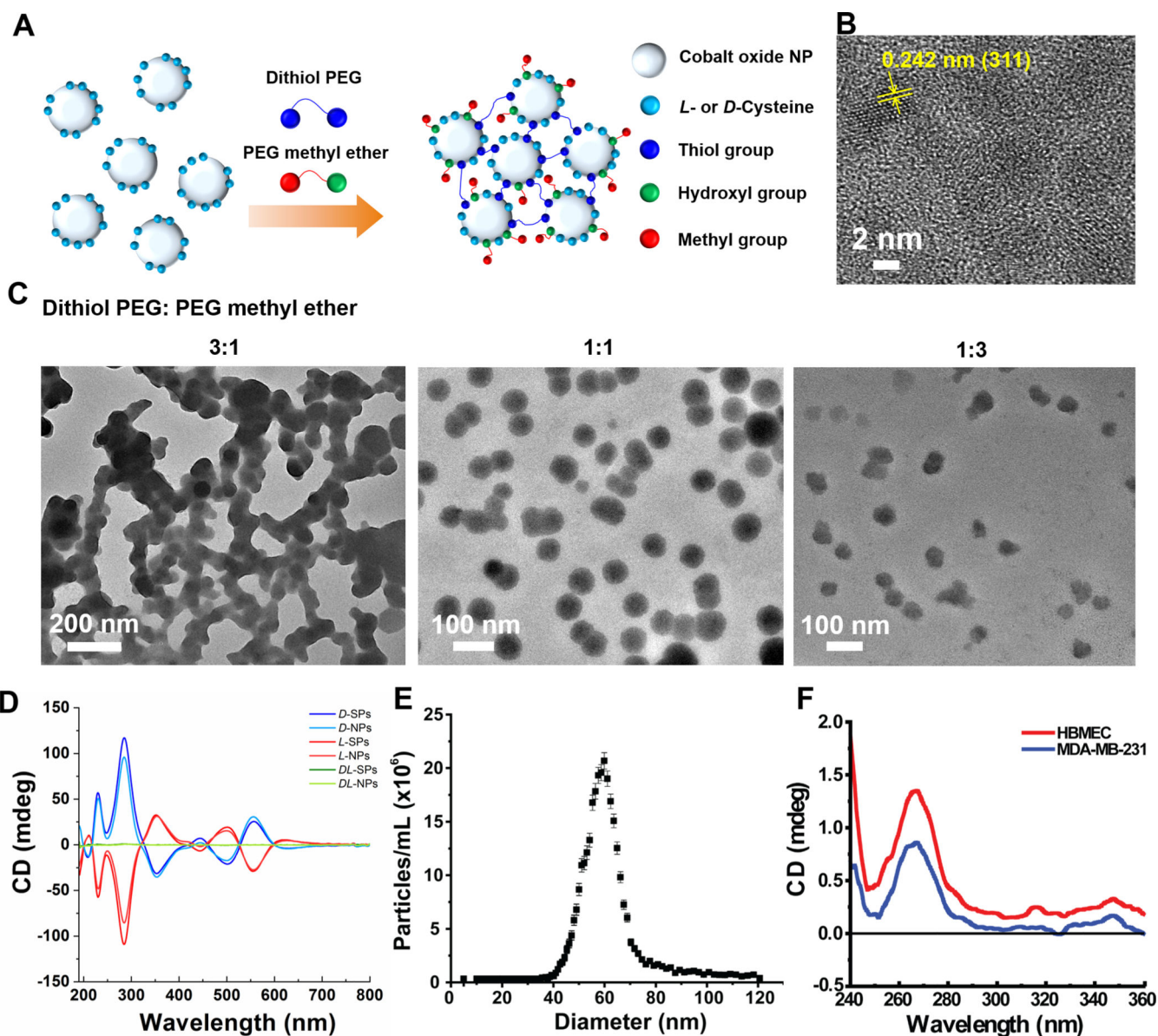[50]. Liu G, Zhang G, in QCM-D Stud. Polym. Behav. Interfaces, SpringerBriefs In Molecular Science, 2013.

Figure 1. Formation of chiral SPs.

A) Schematic illustration of chiral NPs self-assembly into SPs. The building block NPs possess chirality transferred from *L*- or *D*- cysteine on the surface. Due to the strong affinity of thiol groups to cobalt, dithiol PEG works as a cross linker. Hydroxyl group also binds on the NPs surface when methyl group is exposed and then provides slight repulsive force. When the attractive and repulsive interactions are balanced, SPs cease the growth. **B)** HR-TEM image of *L*-SPs. **C)** TEM image of *D*-SPs. **D)** CD spectra of *L*-, *D*-, and *DL*-SPs and *L*-, *D*-, and *DL*-building block NPs. **E)** Nano-flow cytometry measurement of *L*-SPs. **F)** CD spectra of lipids extracted from human bone marrow endothelial cells (HBMEC) and breast cancer cells (MDA-MB-231).
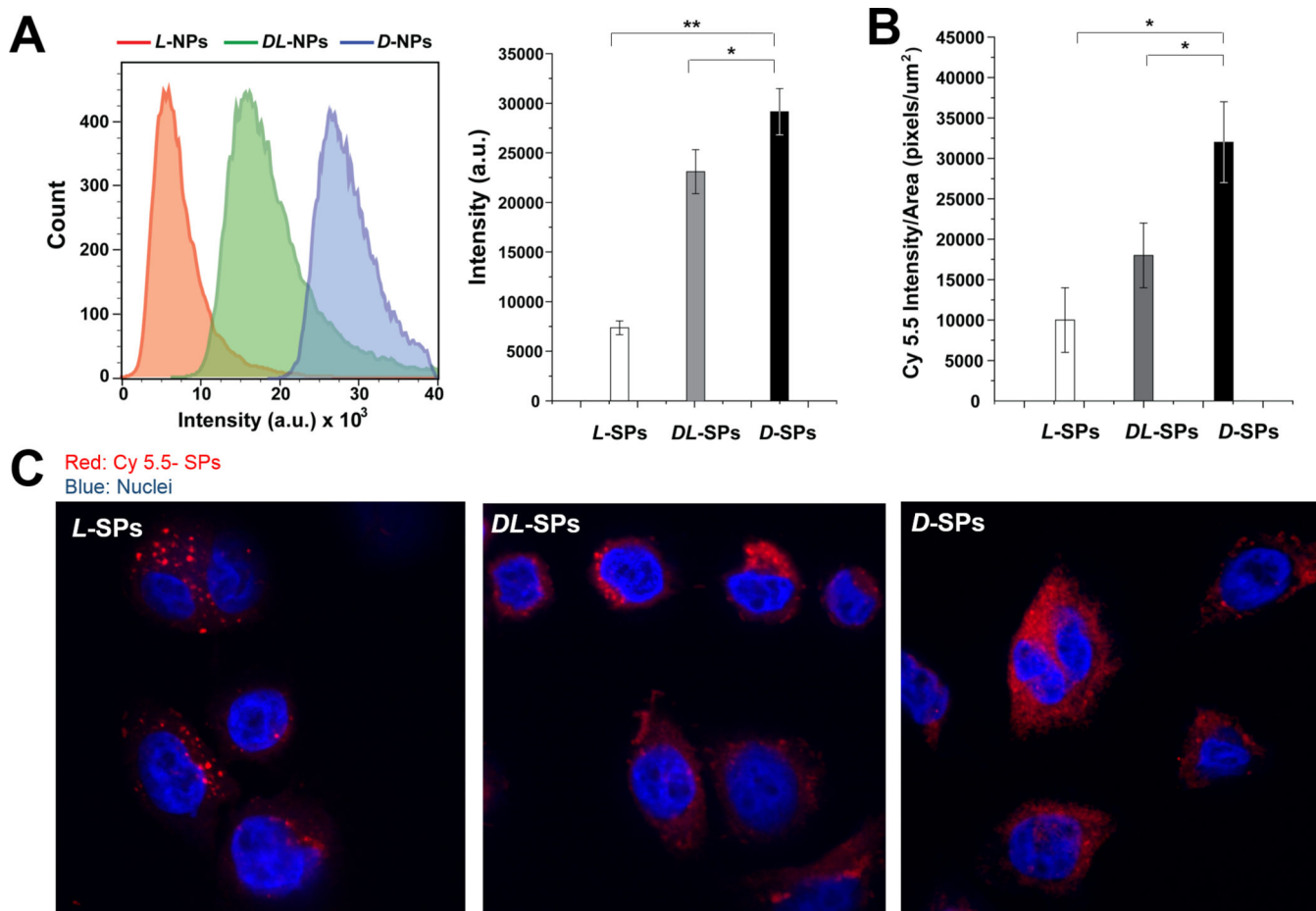
Figure 2. Cell internalization of SPs depending on chirality.
A) Emission intensity of MDA-MB-231 cells treated with fluorescent dye conjugated SPs measured by flow cytometry. Total 10000 cells was counted. **B**) Average red channel intensity from corresponding confocal images. **C**) Confocal images of HeLa cell nuclei (blue) and internalized *D*-, *L*-, and *DL*- SPs (red) corresponding to B. Error bars indicate standard deviation. $*p$ ⩽ 0.05, $**p$ ⩽ 0.001 were calculated using one way anova.
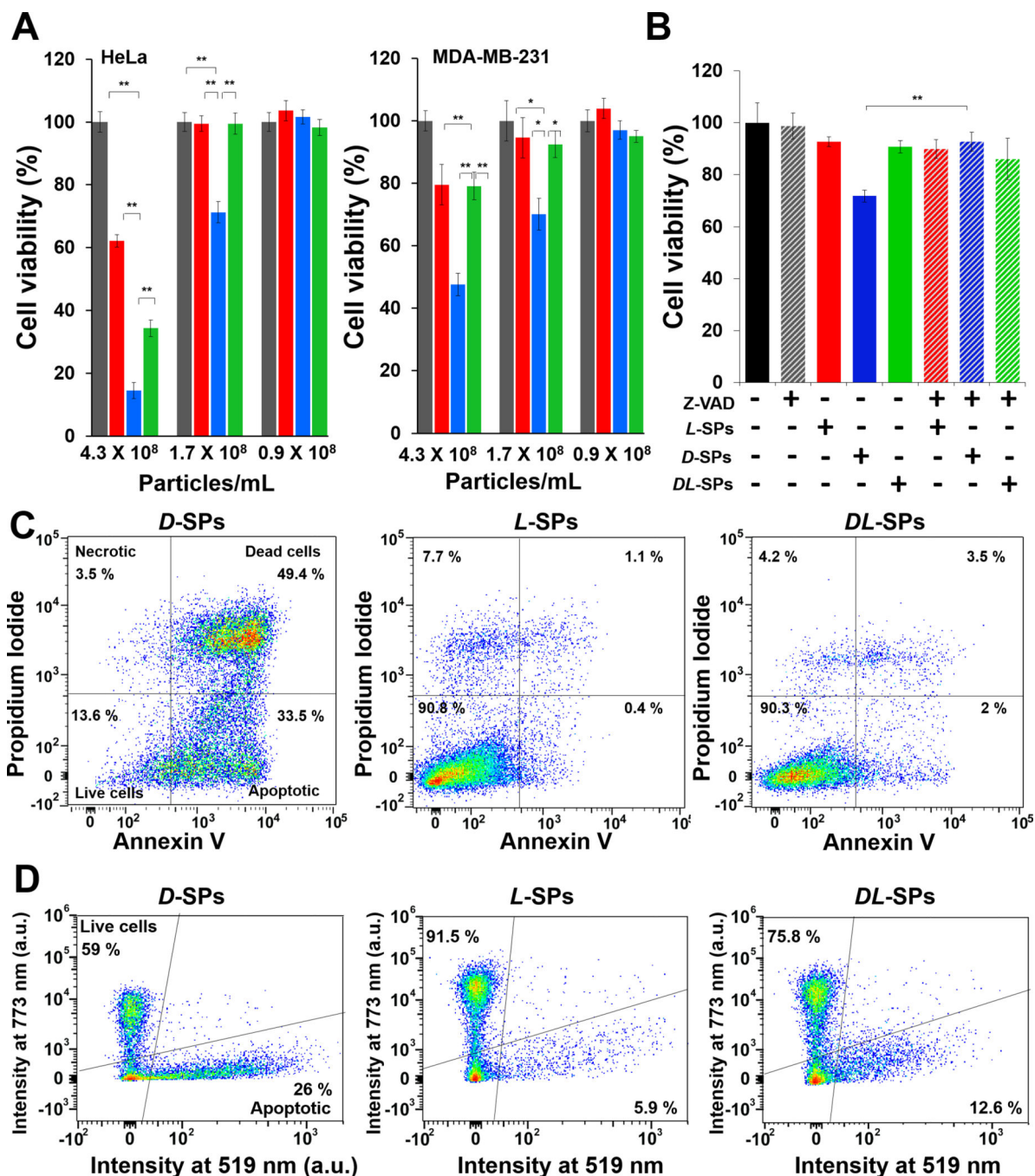
Figure 3. Cell viability and death mechanism against chiral SPs.
A) Cell viability study using HeLa and MDA-MB-231 cancer cells. With the various cell lines including MM. 1S and SKBR3 (Figure S2), *D*-SPs (blue) showed the highest toxicity than *L*- (red) or *DL*- (green) SPs. The grey bars are controls. **B)** Viability analysis of cells treated with SPs with and without prior caspase inhibitor (Z-VAD) treatment using HeLa cancer cells. With Z-VAD treatment, cell viability increased even with *D*-SPs treatment (blue/white bar). C) Annexin-PI analysis after 48-hour incubation of HeLa cells with *D*-, *L*-, and *DL*-SPs using flow cytometry. *D*-SPs treatment caused significant cell death through

apoptosis, while *L-* and *DL*-SPs did not affect cell viability. **D)** Mitochondria membrane potential-dependent fluorescent signals after HeLa cell treatment with *D-* , *L-* , and *DL*-SPs. These results indicate that *D*-SPs induce apoptosis through mitochondria membrane damage, which causes caspase-3 activation. Error bars indicate standard deviation. *p 0.05, **p 0.001 were calculated using one way anova.
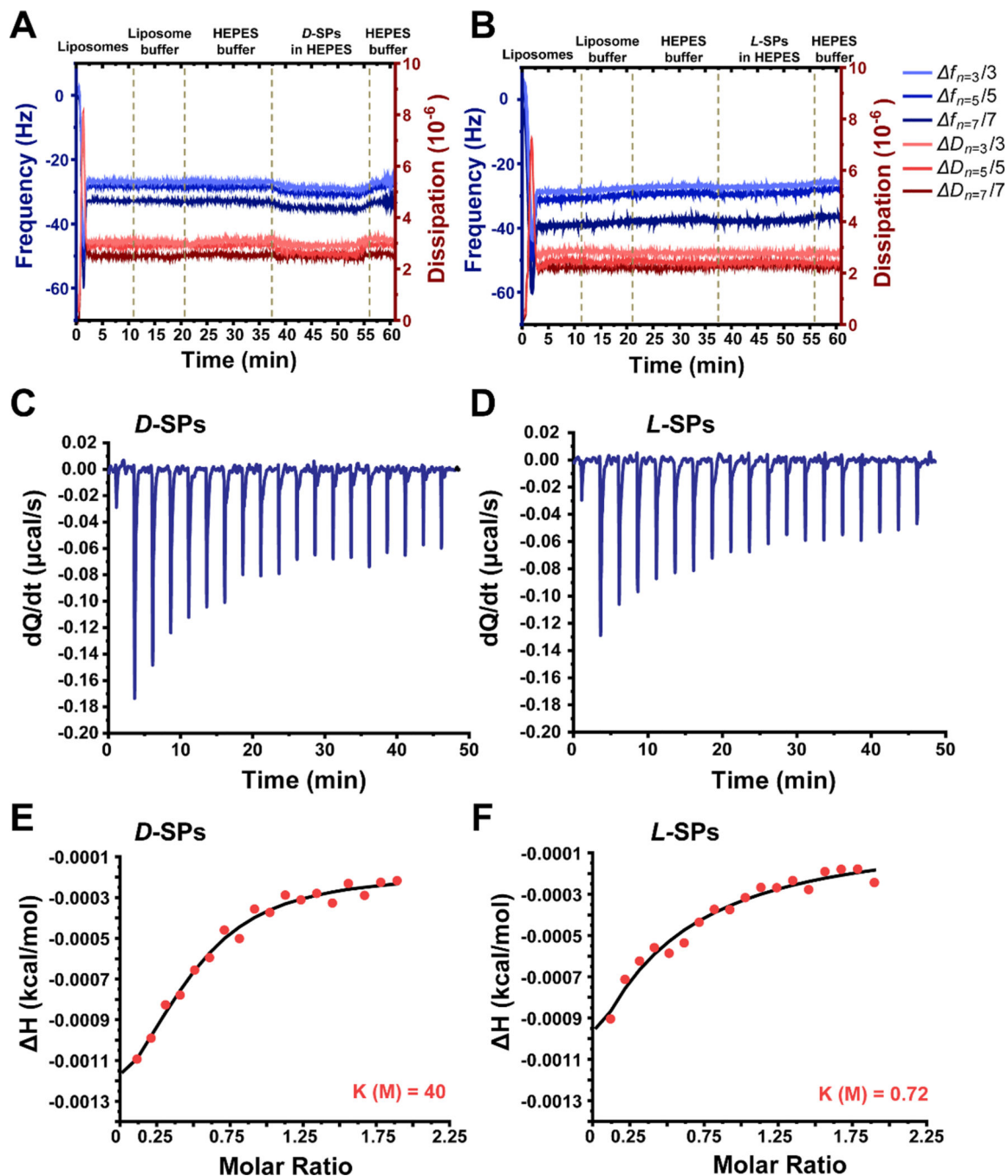
Figure 4. Chiral-specific interaction mechanism.
A and B) QCM-D monitoring of SLB formation and *D*- (A) or *L*- (B) SPs adhesion on quartz crystals over time. The decrease in frequency and dissipation indicates absorption of SPs on SLB. **C-F)** ITC experiments for *D*- (C and E) and *L*- (D and F) SPs in 800 nm liposome dispersions. The association K value of *D*-SPs to liposomes was 56 times higher than that of *L*-SPs.
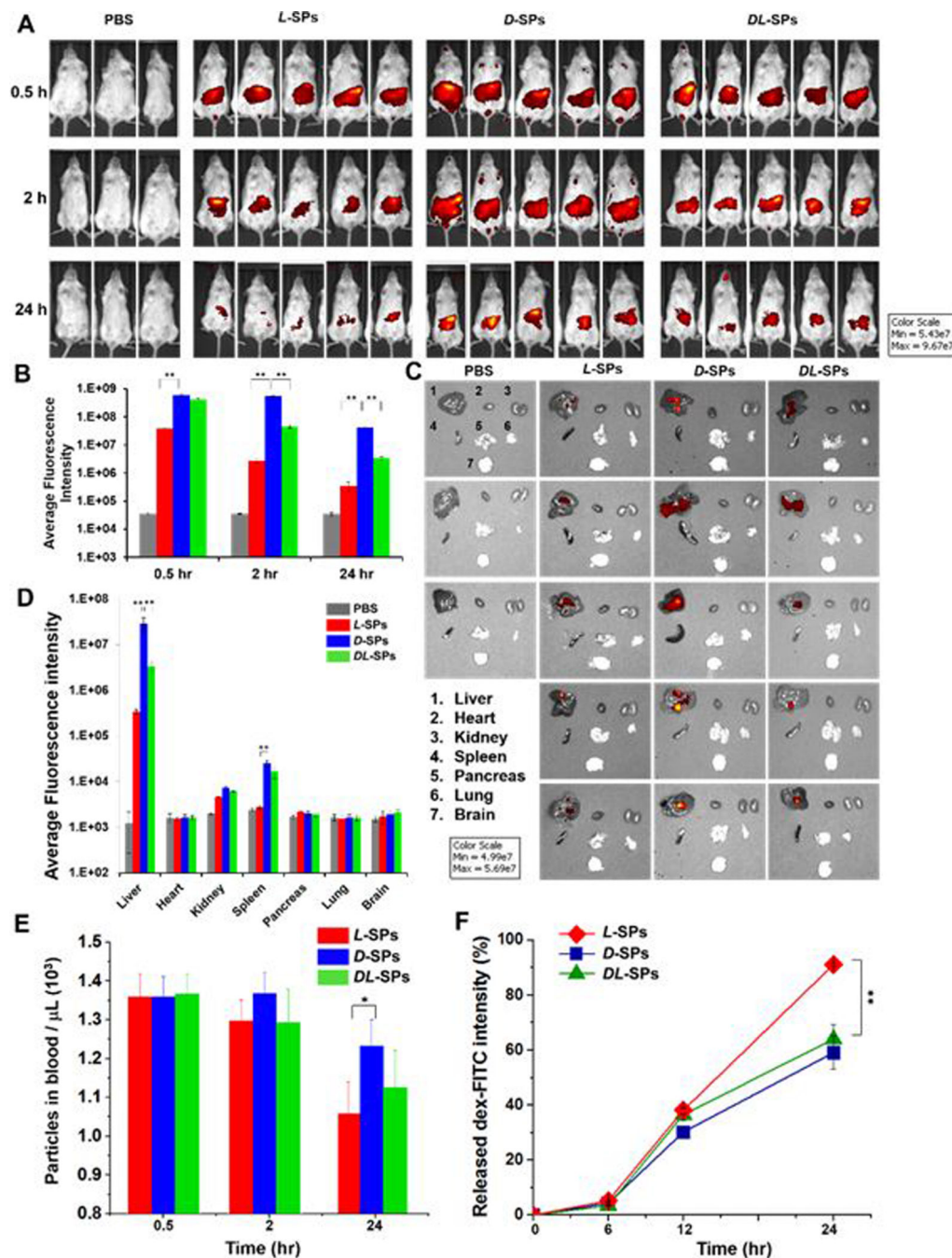
Figure 5. Chiral-specific stability of SPs *in vivo* and *in vitro*.
A) IVIS images of four groups of mice before and after IV injection of PBS buffer, *L*-, *D*-, and *DL*-SPs. **B)** Average fluorescent intensities from dye covalently conjugated to SPs. The grey, red, blue, and green bars are corresponding to PBS, *L*-SPs, *D*-SPs, and *DL*-SPs respectively. **C)** Emission signals from the dye covalently conjugated on chiral SPs. Three or five mice from each group were harvested after 24 hours post injection. *D*-SPs injected mice showed the highest signal while *L*-SPs injected mice had the lowest. The signal from *DL*-SPs injected mice had intermediate intensity between *D*- and *L*-SPs. **D)** Average fluorescent

intensity from harvested organs corresponding to (C). Error bars represent standard deviation. **E)** The number of chiral SPs remained in blood at various time points post injection. *L*-SPs showed the fastest decrease in signal in the blood. **F)** The percentage of released dextran-FITC from chiral SPs after incubation over time in human plasma at 37 °C. *L*-SPs showed the fastest degradation that supports the observed higher body clearance *in vivo* compared to *D*-SPs. *p 0.05, **p 0.001 were calculated using one way anova.